JATIS Journal of Astronomical Telescopes, Instruments, and Systems

RESEARCH PAPER

Accounting for material property uncertainty in the preliminary vibration analysis of opto-mechanical systems

Edoardo Dalla Ricca,[a,b,*,†] **Carlo Zanoni**,[a,b,*,†] **and Edoardo Maria Alberto Redaelli**[c]

[a]University of Trento, Department of Industrial Engineering, Trento, Italy
[b]Italian National Institute for Nuclear Physics, Trento, Italy
[c]Italian National Institute for Astrophysics, Milano, Italy

---

ABSTRACT. The dynamical behavior of opto-mechanical systems is crucial for ensuring the performance in noisy environments. In particular, vibration mitigation is one of the design drivers for pointing and wavefront error requirements. During the initial development stages, the typical design process is based on nominal material properties, geometries, and interface behaviors, resulting in a unique set of frequency response functions. However, this approach lacks robustness and often necessitates extensive redesigns following initial testing or the use of significant margin factors. Conversely, incorporating deviations from the baseline in a statistical manner is computationally heavy and often constrained by confidentiality issues. We give an overview of the most common techniques that can be used in large projects to account for the uncertainty in material properties. We also present a computationally light method aimed at deriving a robust family of system responses via a simple relationship between uncertainties in material properties and system responses. The proposed method is also applicable to models in a modal space representation. We compare a few parametric methodologies that account for material property uncertainties in a rigorous way, showcasing their use with real opto-mechanical systems for both ground and space telescopes. We show that the simplified method yields results comparable to more complex algorithms, offering a practical solution for early-stage design considerations.

Keywords: uncertainty propagation; early design; optomechanical systems; vibrations; material properties; model uncertainty factor

Paper 24096G received Jul. 4, 2024; revised Aug. 28, 2024; accepted Sep. 12, 2024; published Oct. 11, 2024.

---

1 Introduction

Opto-mechanical systems are at the heart of many advanced instruments, encompassing a diverse range of applications, including astronomy,[1,2] fundamental physics,[3] Earth observation,[4] and communication. These systems integrate optical components with mechanical elements, forming complex and delicate hardware that demands meticulous design, fabrication, and operation. However, despite significant heritage and advancements in analysis, uncertainties regarding design remain inevitable and can manifest in various forms, imposing critical challenges on the performance and reliability of these systems. Uncertainties in opto-mechanical systems can arise

---

[*] Address all correspondence to Carlo Zanoni, carlo.zanoni@infn.it; Edoardo Dalla Ricca, edoardo.redaelli@inaf.it

[†] These authors are equal first authors.

from geometrical, material, environmental, and operational variations and can adversely affect the overall performance.

If we consider a mechanical system and build several copies, we would note that, given a certain frequency response function (FRF), its realizations are rather consistent at low frequencies and diverge in high bands where there is a high modal density.[5] The dispersion in this range can be tackled with statistical energy analysis (SEA) techniques.[6] At low frequencies, the dispersion is instead more deterministic and can be foreseen with a model, knowing the deviation of the value of the physical parameters. Such parameter uncertainty can be tackled directly with the finite element method (FEM) by running large sets of statistical simulations. However, obtaining large realizations of FRFs from a high-accuracy FEM model can become prohibitive,[7] and in large projects in which dynamic sub-models are often exchanged in a reduced formulation, the link between parameters and dynamic response is lost.

The presence of uncertainties is then one of the reasons for the use of margin factors. For computational efficiency and agility, the design is made considering nominal parameters and including margins, particularly in hardware that relies on precise optical path lengths or has tight constraints for modal decoupling. Margins mitigate the risk of non-compliance happening later during system implementation but lead to sub-optimal design solutions and lack a statistical meaning.

Varying system parameter uncertainties can lead to non-compliance when shifting eigenfrequencies across distinct bands. In Ref. 8, a frequency-dependent vibration requirement case for an extremely large telescope (ELT),[9] optical system is presented. This example demonstrates requirement compliance variability reaching up to a factor of 3× with abrupt transitions attributed to control systems cutoffs. A robust design and analysis are thus crucial.

Recent works[10–13] have investigated the issue of uncertainty of micro-vibrations in spacecraft and proposed the modified Craig-Bampton method. The Craig-Bampton method[14] is one of the classical tools for dynamic sub-structuring, particularly common in aerospace, in which different entities with competing commercial interests are working on separate subsystems. The proposed modified Craig-Bampton allows for accounting for a measured variability in the modal response via a randomization of the natural frequencies and the modal participation factors of the subsystems. This technique accelerates the generation of a family of random systems and FRFs to be used in the analysis when necessary.

The effects of deviations of material and geometric parameters on the variability of a vibration transfer function of a simple structure are shown in Ref. 15, but without providing possible strategies on how to tackle them during the development phase.

Uncertainty plays a crucial role in all space hardware that is coupled to a rocket during launch. The launch environment is one of the key design drivers, dictating modal and structural requirements. In Refs. 16–18, reviews of the challenges posed by the uncertainty are presented, providing qualitative examples and describing the management and technical limitations of tackling the issue. In this regard, Ref. 19 shows how unrepresentative structural predictions may lead to overtesting.

Reference 20 uses a clever combination of numerical models with different fidelity levels to quantify the effects of parametric uncertainty in the design of complex, large-scale, multidisciplinary systems such as the James Webb Space Telescope. This methodology relies on the availability of physical models and follows a Monte Carlo approach, although with a much more efficient strategy than the simple brute-force with high-fidelity simulations.

A common approach to uncertainties is the use of margin a model uncertainty factor as described in Ref. 21. However, this approach heavily relies on previous engineering knowledge, which may not always be available.

In general, uncertainty quantification and propagation have been extensively investigated for various engineering systems and processes.[22–24] With the Monte Carlo approach, it is possible to perform uncertainty quantification also on large-scale projects.[20,25] This is, however, limited by the real availability of physical models and can be computationally intensive. The use of other modern methodologies in large-scale projects is often impractical.[26]

With this paper, we aim to provide the technical community with hands-on tools that represent a step forward in the design practice, avoiding the complexities of the most recent methods and the over-simplification of margin factors. In particular, the final goal is an approach that does not require the availability of detailed physical models and lengthy simulations. A corner reference for our paper is Ref. 27, which derives a local expansion-based method to link the uncertainty of design parameters to an FRF realization. It introduces the use of an error propagation approach in which a small change in a system parameter is mapped to a change in eigenfrequencies and eigenmodes. We take the method of Ref. 27 and further investigate and streamline it. We then propose a completely new approach that, due to a simplified relationship between uncertainties in material properties and system responses, allows for deriving a robust family of system's responses that, given a nominal FRF, requires no additional FEM simulations and limited knowledge of the system. This approach also avoids issues related to confidentiality constraints, which limit the availability of physical models, and can be used with reduced and modal representations.

We focus on the opto-mechanical systems not only because they are often sensitive to vibrations, both on-ground and in space, but also because they have recurrent features that help to define a common approach. Recurrent features are related, for example, to the similarity of a mirror cell to a cantilevered beam with a mass at its extremity. This topological analogy allows us to propose and validate a general relationship between material property uncertainty and a system's response envelope. This link is useful especially in the early design phase, when there are no measured data available.

The article is organized as follows. In Sec. 2, we review four methods suitable to the generation of random systems based on parameter uncertainty, including our proposals. In Sec. 3, we introduce three real opto-mechanical designs, and in Sec. 4, we apply the four methods to them to assess their performance. In Sec. 5, we draw some conclusions and discuss future developments.

2 Methods

Accounting for parameter uncertainty in the preliminary design means being able to link a known stochastic value of key material and geometrical properties to either a random set of FRFs, to be used in dynamical simulations, or a robust FRF definition that at each frequency gives a conservative amplification factor, which typically means a higher amplification. In other words, a curve that envelops all of the expected FRF realizations.

We focus here on the material properties, such as Young's modulus and density. Geometric properties are more system specific but can be tackled with the methods described altogether.

2.1 Deterministic Finite Element Monte Carlo Method

In the mid-to-low frequency band, the modal behavior is deterministic. The deterministic finite element Monte Carlo (DFEM) method is able to foresee the dynamic of a given system. The limitation of this approach is that, to derive a large number of realizations of system responses, many simulations need to be performed with a significant computational burden.[7]

Focusing on the material properties, given the system parameter p (e.g., Young's modulus), we run modal simulations randomizing p with a Gaussian distribution in a Monte Carlo fashion. For each iteration, we build a dynamic model and obtain the FRFs at all points of interest, allowing for a statistical treatment of the output. Given the deterministic nature of the problem, we consider these results as the benchmark. It goes without saying that, in a typical development process, the designer also needs to account for model inaccuracies, such as the stiffness of an interface.

Estimating an FRF in each finite element simulation is a heavy computational task. To facilitate this step, we use a model reduction approach based on the typical modal superposition.[28,29] The complete procedure is as follows:

1. Perform the modal analysis of the ith realization of the system with the ith value of the parameter p to be randomized.
2. Export j (user-defined value) natural frequencies and mode shapes for each simulation. The mode shapes are evaluated in a subset m (user-defined value) of selected points of the model considered of interest, each one having 6 degrees of freedom (DoFs). These points can either be nodes of the meshed volume or remote points linked to surfaces with a rigid

body connection with either a deformable or rigid formulation. In the deformable case, the points provide the average position and attitude values of the attachment nodes.

3. Given the ith simulation results, write the model dynamics in state space representation. To do so, we name $x_i(t)$ the following vectors:

$$x_i(t) = \{x_{1,i}(t), x_{2,i}(t)\}^T = \{q_i(t), \dot{q}_i(t)\}^T, \tag{1}$$

where $q_i(t)$ is the vector containing the j solutions to the model equations of motion in modal coordinates assuming constant damping ratio ζ, i.e.:

$$\ddot{q}_i(t) + 2\zeta\omega_{n,i}\dot{q}_i(t) + \omega_{n,i}^2 q_i(t) = \Phi_i^T F, \tag{2}$$

where F is the vector containing the $6m$ inputs to the system, $\omega_{n,i}$ is the $j \times j$ matrix containing the j natural frequencies of the ith simulation along the diagonal, and Φ_i is the $6m \times j$ mode shapes matrix of the corresponding model, i.e.,

$$\Phi_i = \begin{bmatrix} \phi_{1,1,1} & \dots & \phi_{1,1,j} \\ \dots & \dots & \dots \\ \phi_{1,6,1} & \dots & \phi_{1,6,j} \\ \dots & \dots & \dots \\ \phi_{m,1,1} & \dots & \phi_{m,1,j} \\ \dots & \dots & \dots \\ \phi_{m,6,1} & \dots & \phi_{m,6,j} \end{bmatrix}, \tag{3}$$

where $\phi_{m,z,j}$ is the mode shape evaluated at the zth DoF ($z \in \{1, \dots, 6\}$) of the mth point for the jth frequency.

To express the output displacements as functions of the input displacements $u(t)$, it is possible to write the force $F(t)$ as

$$F = ku(t), \tag{4}$$

where k is a spring with a constant stiffness and is used to replicate seismic shifts between the ground and the structure.

As a result, the state space representation becomes

$$\dot{x}_i(t) = A_i x_i(t) + kB_i u(t) \quad y_i(t) = C_i x_i(t), \tag{5}$$

where $y_i(t)$ represents the displacements at the desired points in the physical space, $\dot{x}_i(t)$ is the state space vector, and matrices A_i, B_i, and C_i are equal to

$$A_i = \begin{bmatrix} 0 & I \\ \begin{bmatrix} \backslash & & \\ & -\omega_n^2 & \\ & & \backslash \end{bmatrix} & \begin{bmatrix} \backslash & & \\ & -2\zeta\omega_n & \\ & & \backslash \end{bmatrix} \end{bmatrix}, \tag{6}$$

$$B_i = \begin{bmatrix} 0 \\ \Phi_i^T \end{bmatrix}, \tag{7}$$

$$C_i = [\Phi_i \quad 0], \tag{8}$$

where 0 and I are the $j \times j$ null and identity matrices, respectively.

4. Write the state space representation in the Laplace domain assuming zero displacement and velocity in the derivation:

$$s\tilde{x}_i = A_i\tilde{x}_i + kB_i\tilde{u} \quad \tilde{y}_i = C_i\tilde{x}_i, \tag{9}$$

where s is the complex variable and $\tilde{x}_i$, $\tilde{y}_i$, and $\tilde{u}$ are the Laplace transform of $x_i(t)$, $y_i(t)$, and $u(t)$, respectively.

5. Compute the transfer functions between the state and the input displacements and between the output and the input displacements, respectively, as

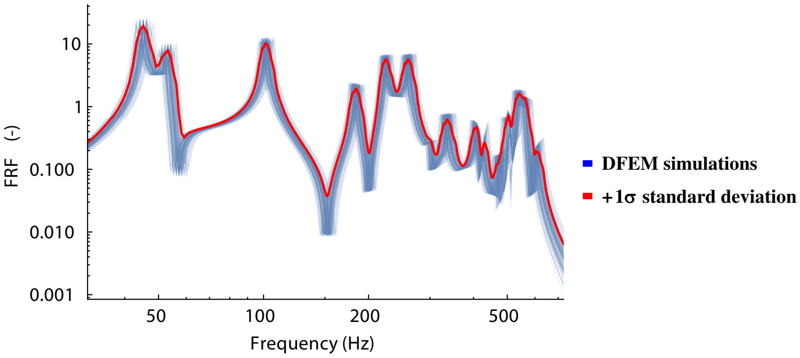

Fig. 1 Example results of the DFEM. The method is applied considering a standard deviation of Young's modulus of 5%. The red curve is the $+1\sigma$ standard deviation of the generated points at each frequency.

$$G_i(s) = k(Is - A_i)^{-1}B_i, \tag{10}$$

$$H_i(s) = kC_i(Is - A_i)^{-1}B_i, \tag{11}$$

where $G_i(s)$ and $H_i(s)$ are vectors with dimensions that are equal to the total number of DoFs of the system (i.e., $6m$).

6. Extract the FRFs at the DoFs of the desired points.

In Fig. 1, we show a family of FRF curves generated with the DFEM method applied to one case study detailed in Sec. 3. The FRFs are extracted at one point in the structure considering a Gaussian distribution of Young's modulus with a normalized standard deviation of 5%. The red curve is the $+1\sigma$ standard deviation at each frequency. This $+1\sigma$ curve can be used as a conservative FRF for further performance analyses.

2.2 Modal Propagation

In a modal representation, a change in a system parameter p (e.g., Young's modulus) results in variations in matrices ω_n and Φ. The variations can be linearized according to Eqs. (12) and (13),[27] providing a direct link from a parameter uncertainty (δp) to model uncertainties ($\delta\omega_n$ and $\delta\Phi$):

$$\delta\omega_n = \frac{\partial\omega_n}{\partial p}\delta p, \tag{12}$$

$$\delta\Phi = \frac{\partial\Phi}{\partial p}\delta p. \tag{13}$$

In this case, two FE simulations are necessary: one simulation is run in the nominal configuration of the system and one with a small (e.g., 1%) variation in p. The simulations provide the desired link from parameter uncertainty to model uncertainties, i.e., $\delta\omega_n$ and $\delta\Phi$. Given a Gaussian distribution of the parameter δp, we can randomize the nominal model by perturbing natural frequencies and mode shapes together according to Eqs. (12) and (13). The derivation of the corresponding FRFs is then straightforward.

The modal propagation method (MP) is computationally lighter than the DFEM method, but it still leaves room for some further simplification and computational time saving. The use of the mode shapes coupled with the modal frequencies is not easy to interpret until final results are obtained and does not provide a general forecasting relationship between parameters and response functions.

2.3 Frequency Propagation

The frequency propagation method (FP) is the first of our proposals, and it is simply derived from the MP: the uncertainty δp is propagated to $\delta\omega_n$ with Eq. (12), but neglecting the effect on the mode shapes of Eq. (13), which becomes

$$\delta\Phi \approx 0. \tag{14}$$

If the stiffnesses of a system change all proportionally, the modal shapes do not change. Only the eigenfrequencies do. This can be seen in a straightforward way in a lumped model with springs and masses.

Pragmatically, the proportional change of stiffnesses is justified in the case of a support structure for which we can suppose the main material is one and is probably coming from the same supplier and same batch. Therefore, the uncertainty is correlated in all its parts. Deviations due to parts in other materials or different origins are supposed to be a second-order effect.

Given a Gaussian distribution of the parameter δp, we can randomize the nominal model by perturbing natural frequencies according to Eq. (12).

This method is simple and easy to interpret, but it still lacks a generic relationship between parameters and response functions. The link of Eq. (12) is derived on a case-by-case basis.

2.4 Frequency Envelope Perturbation

The frequency envelope perturbation method (FEP) is the second of our proposals and is well explained considering an analogy with a cantilevered beam of length l subjected to a concentrated mass m at its free end. The beam static deflection y due to gravity is equal to[28,29]

$$y(l) = \frac{mgl^3}{3EI}, \tag{15}$$

where E and I are the beam Young's modulus and moment of inertia, respectively, and g is the gravitational acceleration.

The first natural frequency of the beam is[28,29]

$$\omega_1 = \sqrt{\frac{3EI}{ml^3}}. \tag{16}$$

In a modal representation, a change in system parameter p results in a change in ω_1. The change in frequency due to a change in the beam Young's modulus $\frac{\delta\omega_1}{\delta E}$ is equal to

$$\frac{\delta\omega_1}{\delta E} = \frac{\sqrt{3\,\frac{EI}{ml^3}}}{2E}. \tag{17}$$

Rearranging the terms above, we derive

$$\frac{\delta\omega_1}{\omega_1} = \frac{1}{2}\frac{\delta E}{E}, \tag{18}$$

which links the standard deviation of the natural frequency to one of Young's moduli.

Extrapolating this result to a generic opto-mechanical system, we can generate a family of FRF due to uncertainties by randomizing the frequencies of the modes according to the factor 1/2. It is worth noting that this factor applies to all parameters that have a square root proportionality to a natural frequency. The cantilevered beam is thus only a meaningful example. An extension of the application of the FEP beyond Young's modulus is the mass of a system, which is typically underestimated in early development. This is further discussed in Sec. 4.3.

The advantages of this method are that it provides a clear link between uncertainty and dynamic behavior and that it does not require lengthy numerical calculations. To the best of our knowledge, the FEP is not used in the design of mechanical systems.

3 Case-Study Systems

The four proposed methods are tested on three case studies. The first two cases concern subsystems taken from MORFEO,[30] a $7 \times 8 \times 4$ m key instrument for the adaptive optics of the ELT that will use two deformable mirrors to correct for different layers of turbulence in the atmosphere (see Fig. 2). The third case is a concept of the optical assembly in the LISA space mission. LISA will be the first gravitational waves observatory in space, covering the 0.1 mHz to 1 Hz band with a constellation of three satellites in a triangular formation (see Fig. 3). The three cases are explained in the following. In all models, we assume a damping ratio, ζ, of 0.75%.

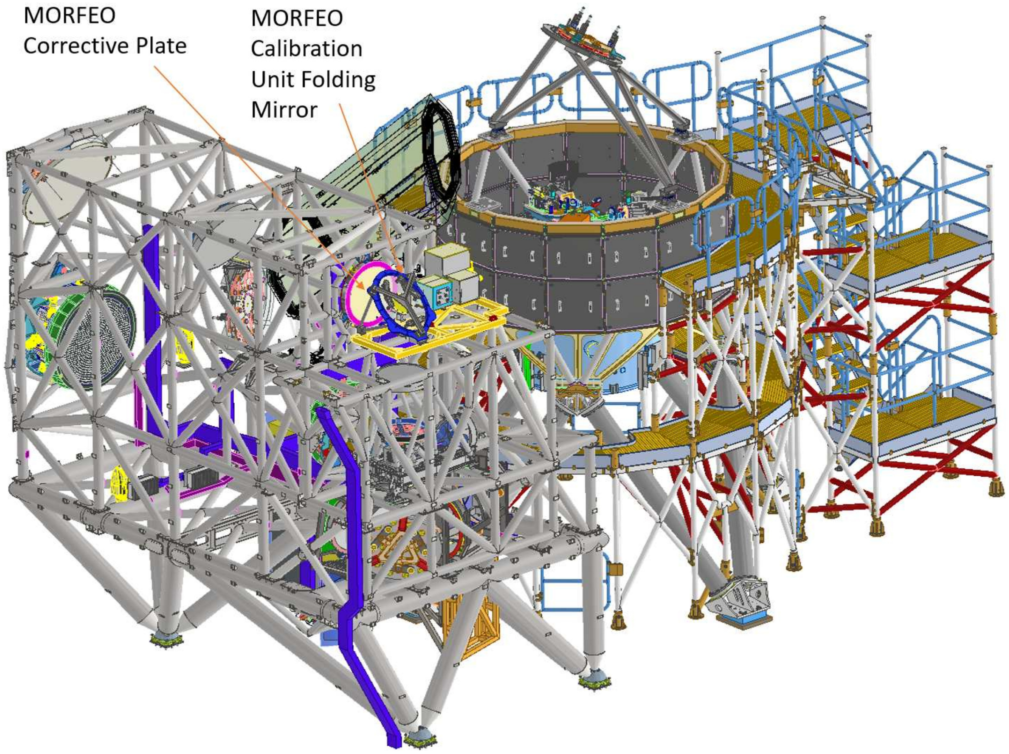

Fig. 2 Rendering of MORFEO instrument. The positions of the two subsystems considered are reported in the figure.

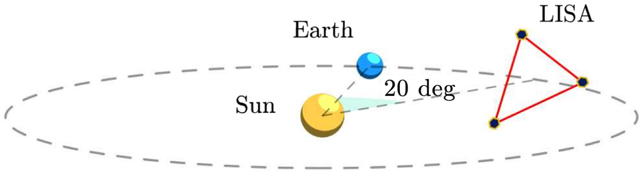

Fig. 3 View of the Earth-trailing LISA constellation (not to scale). The three spacecraft are located on the vertices of the red triangle with a side length of 2.5×10^6 km.

3.1 MORFEO Calibration Unit Folding Mirror

In Fig. 4, we show the first case study for a total weight of 116.85 kg. This mirror has a clear aperture of class 1 m. It is responsible for folding the light from the calibration unit of MORFEO into the instrument. Because we are interested in the FRF between the interface and the mirror, we include a set of remote points in the model (see Fig. 4). These remote points are attached to all locations in which an output displacement or input force is desired, such as the center of the mirror, in this case. A dedicated remote point is connected to the feet of the structure with a standard RBE2 formulation and is linked to the ground with a virtual very stiff spring (stiffness k is $1 \times 9\ \mathrm{N\,m^{-1}}$), which is used to apply a known seismic displacement.

The materials are summarized in Table 1.

3.2 MORFEO Corrective Plate

The corrective plate is shown in Fig. 5. This optical element is an aspherical lens and is the entrance window of the instrument. Similar to the first case, we define a remote point attached to the center of the mirror and one that is linked to the ground via a stiff spring. The total weight of the system is 255.56 kg. This element is the first element in the main optical path of MORFEO.

The materials are summarized in Table 1.

In these subsystems, Young's modulus of the steel is chosen as the parameter affected by uncertainty.

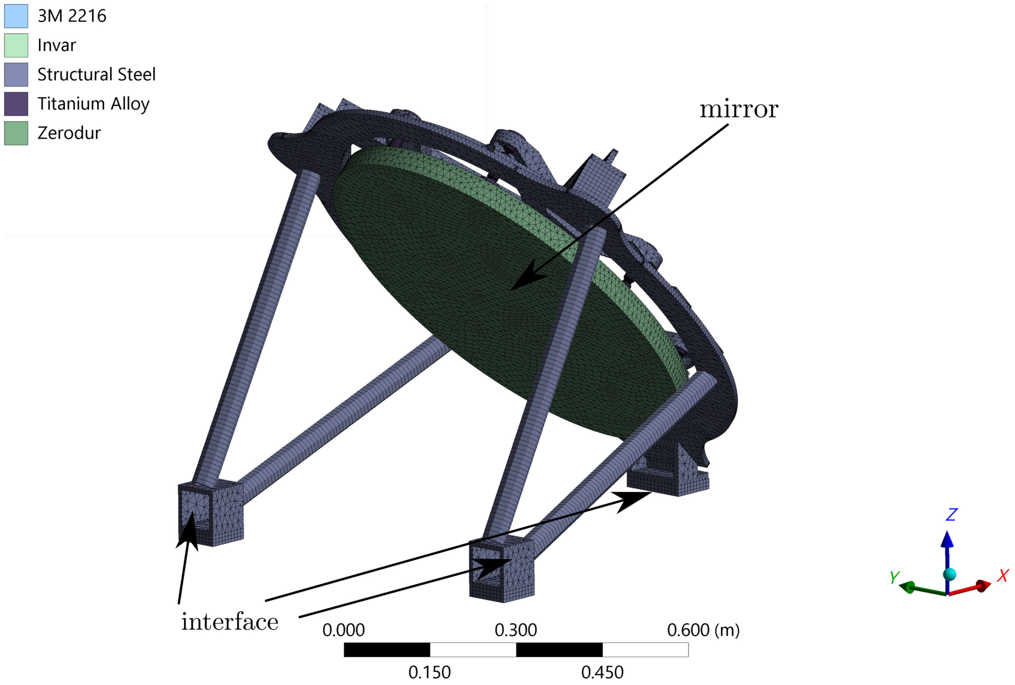

Fig. 4 Rendering of MORFEO CUFM. The ground consists of all surfaces that are either on the ground or connected to other MORFEO subsystems, and the center of the mirror is the point where the FRFs are evaluated.

Table 1 Materials composing the two MORFEO subsystems.

Material	Young's modulus (MPa)
3M 2216	2.95
Invar	150
Steel	200
Titanium alloy	96
Zerodur	91
Fused silica	72.5

3.3 LISA Optical Assembly

In Fig. 6, the third case study is shown. The LISA optical assembly model consists of the following parts:[31]

- The gravitational reference sensor (GRS), which includes the free-falling 1.928 kg cubic-shaped test mass. The total weight of the GRS is modeled as a lumped mass (Fig. 6).
- The optical bench assembly (OBA), which hosts all optical elements combining the signals of the interferometers and includes an optical bench constructed from a block of zerodur glass measuring $200 \times 212 \times 22.5$ mm. The total weight of the OBA is modeled as a lumped mass (Fig. 6).
- The 40-cm off-axis telescope (mechanical length of about 60 cm, a field of view of ± 7 μrad out of the plane and ± 4 μrad in the plane).
- The titanium support structure holding all of the previous systems.

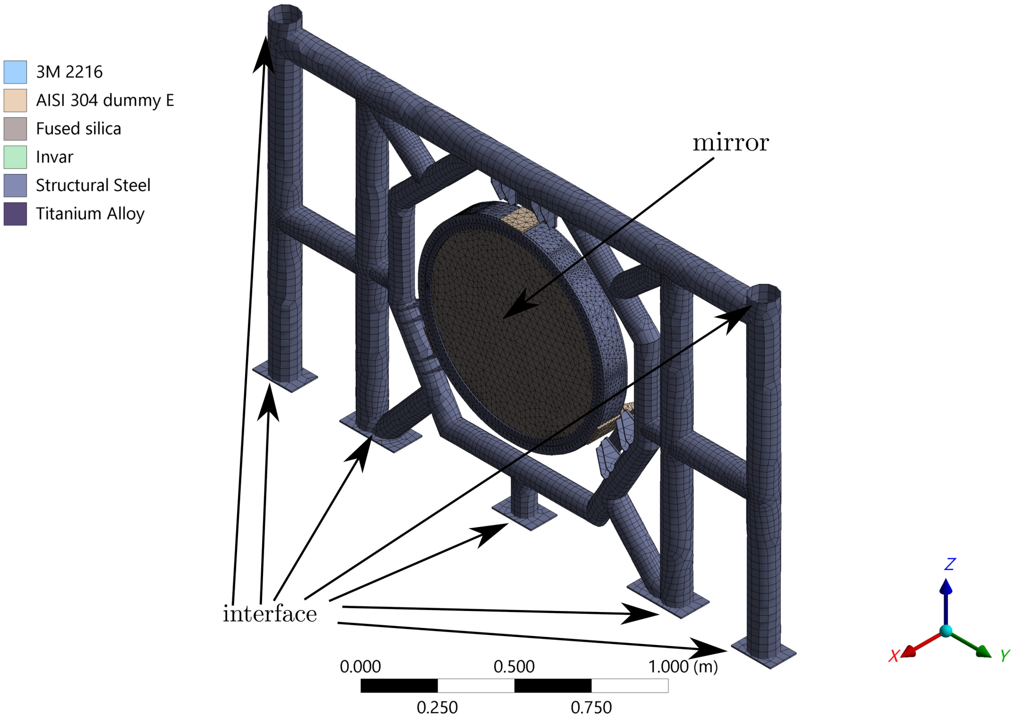

Fig. 5 Rendering of MORFEO CP. The ground consists of all surfaces that are either on the ground or connected to other MORFEO subsystems, and the center of the mirror is the point where the FRFs are evaluated.

Note that the model is only notional and replicates the topology of the LISA optical assembly but does not replicate the dynamic behavior.

Because we are interested in the FRFs between spacecraft and the mirrors, we define remote points as in the previous cases: one on the surface that are directly connected to the satellite and one in the center of the main mirror.

In Table 2, the main materials of the LISA model are summarized.

The methods introduced in Sec. 2 are applied to the LISA optical assembly, varying Young's modulus of the titanium alloy.

4 Summary of Numerical Results

We apply the four methods to the abovementioned three case studies, considering a unitary input displacement to the ground along the x direction, parallel to the mirror's normal direction. To account for uncertainty in Young's modulus, we ran 150 iterations for each method at four different uncertainty levels: 2%, 3%, 5%, and 7% of the nominal value. These values are drawn randomly from a Gaussian distribution. As a result, a total of 7200 simulations are performed. The computational time required to perform a single iteration is on the order of minutes for the DFEM simulation, whereas it is less than a second for the propagation methods.

For each method, the result is a family of curves that we consider the $+1\sigma$ standard deviation curve. We take as a benchmark the equivalent $+1\sigma$ curve of the 150 DFEM simulations. Each FEM model has about 5×10^5 nodes. The use of the $+1\sigma$ curve is arbitrary and for comparison purposes only. Depending on the application, $+2/3/4\sigma$ values should be used.

Figure 7 shows the $+1\sigma$ standard deviation of the FRFs due to a 2% Young's modulus uncertainty level for MORFEO CUFM, MORFEO CP, and LISA optical assembly, respectively. The FRFs are for the input and outputs along the x direction. Similarly, Fig. 8 shows the $+1\sigma$ standard deviation of the FRFs linked to a 7% uncertainty level. In each figure, four curves are plotted together: the blue, orange, black, and red lines refer to the FRFs computed with the FP, MP, FEP, and DFEM methods, respectively. The difference between the curves increases with an increment in Young's modulus uncertainty, especially at high frequencies.

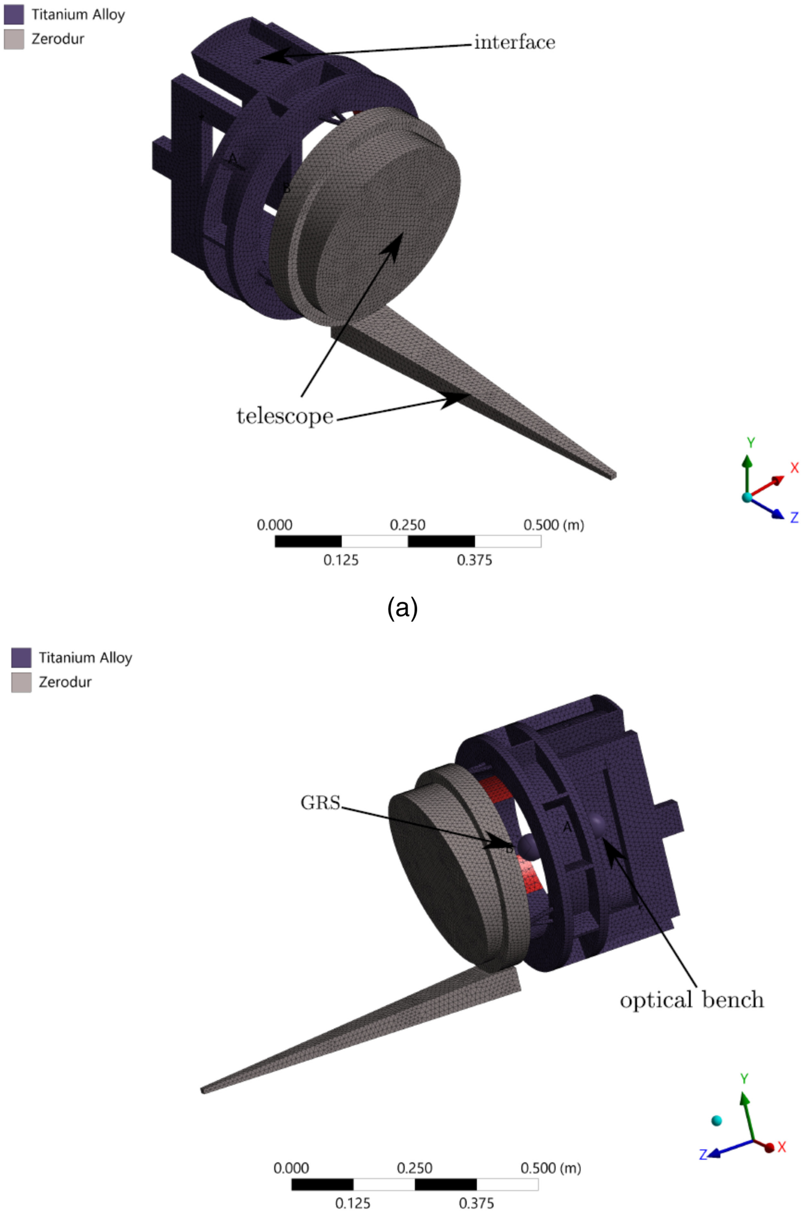

(a)

(b)

Fig. 6 Rendering of LISA's telescope. The interface consists of all surfaces connected to the satellite, and the center of the telescope is the point where the FRFs are evaluated.

Table 2 Materials composing the LISA optical assembly.

Material	Young's modulus
Titanium alloy	96 MPa
Zerodur	91 MPa

To properly assess the results of the proposed methods, we consider two quantitative metrics, testing different aspects of the FRFs being compared:[32] the root mean square error (RMSE) to measure the differences between any two curves (i.e., the accuracy of the methods) and the Pearson correlation coefficient to measure the correlation between any two curves.

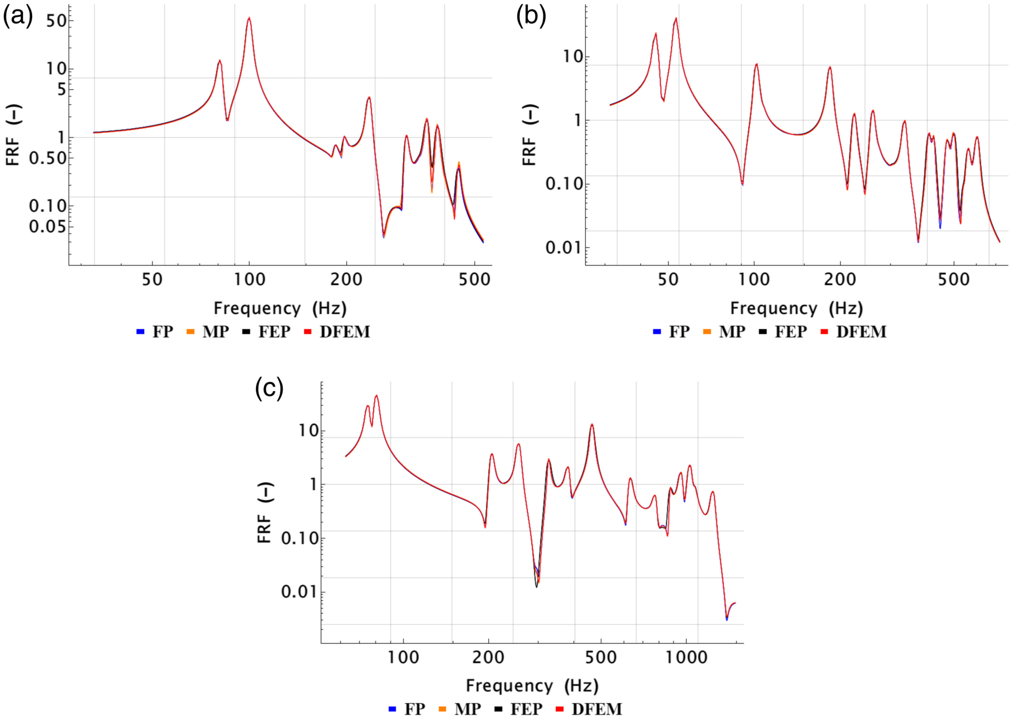

Fig. 7 Mean FRFs summed to their standard deviations along the *x* direction, computed at a 2% uncertainty level. The top left and right charts refer to MORFEO CUFM and MORFEO CP, respectively, and the bottom one refers to the LISA optical assembly. In each plot, four curves are included: the blue, orange, black, and red lines refer to the FRFs computed with the FP, MP, FEP, and DFEM methods, respectively.

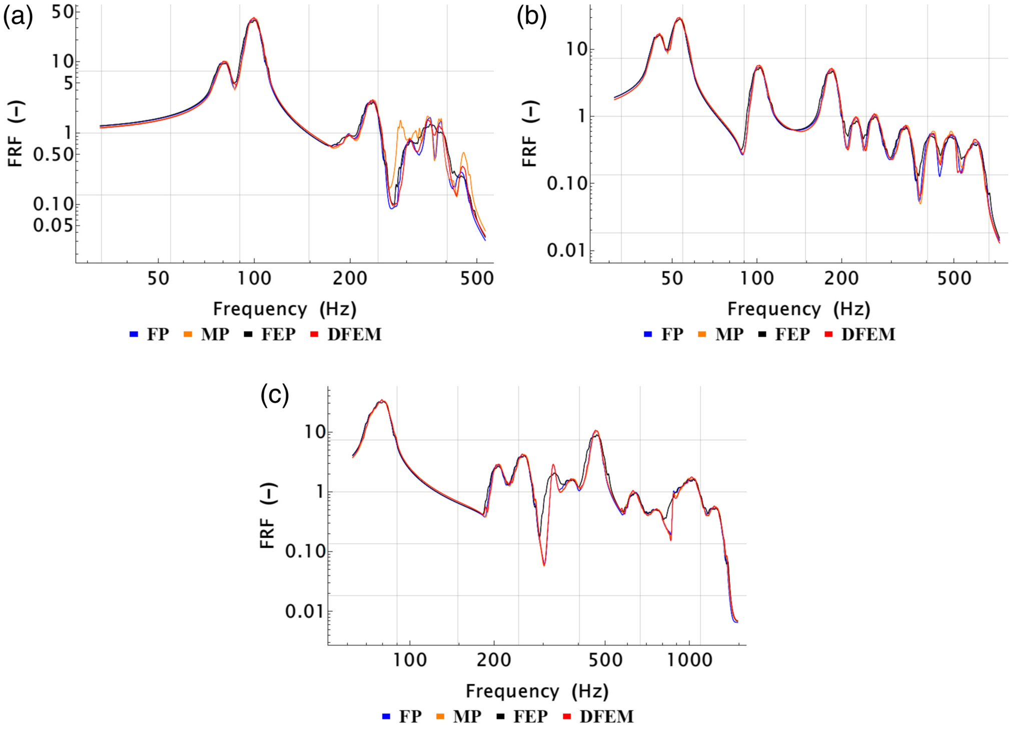

Fig. 8 Mean FRFs summed to their standard deviations along the *x* direction, computed at a 7% uncertainty level. The top left and right charts refer to MORFEO CUFM and MORFEO CP, respectively, and the bottom one refers to the LISA optical assembly. In each plot, four curves are included: the blue, orange, black, and red lines refer to the FRFs computed with the FP, MP, FEP, and DFEM methods, respectively.

4.1 Root Mean Square Errors

The RMSE measures how close two curves are, accounting for biases between them, emphasizing the contribution of larger differences but not considering systematic or random variations between the curves.[32] Given two series a and b that are being compared, the RMSE is defined as

$$\mathrm{RMSE} = \sqrt{\frac{\sum_{n=1}^{L}(a_n - b_n)^2}{L}}, \tag{19}$$

where a_n and b_n are the series values at the n'th sample and L represents the total number of samples. In general, the lower the RMSE value is, the closer the two curves are.[33]

As we chose the DFEM method as the benchmark (see Sec. 2.1), we estimate the RMSE between the DFEM FRF at $+1\sigma$ standard deviation and the MP, FP, and FEP methods, respectively, at the same $+1\sigma$.

Each RMSE value is normalized by the root mean square of the mean FRF computed with the DFEM method, returning three values labeled r_{MP}, r_{FP}, and r_{FEP}.

The ratios are computed at any uncertainty level and are reported in Tables 3 and 4 for MORFEO CUFM, Tables 5 and 6 for MORFEO CP, and Tables 7 and 8 for the LISA optical assembly.

Table 3 Normalized RMSE for MORFEO CUFM, considering the FRFs along the input direction.

σ_E (%)	r_{MP} %	r_{FP} %	r_{FEP} %
2	2.14	2.72	4.49
3	2.72	3.42	5.82
5	5.53	5.99	9.02
7	9.40	9.29	12.30

Table 4 Normalized RMSE for MORFEO CUFM, considering the FRFs along the normal direction.

σ_E (%)	r_{MP} %	r_{FP} %	r_{FEP} %
2	2.49	3.20	5.47
3	3.95	4.66	7.04
5	6.44	7.37	10.47
7	9.14	9.86	13.05

Table 5 Normalized RMSE for MORFEO CP, considering the FRFs along the input direction.

σ_E (%)	r_{MP} %	r_{FP} %	r_{FEP} %
2	2.61	3.84	4.80
3	2.36	3.57	4.65
5	5.40	6.85	8.47
7	9.01	9.63	11.39

Table 6 Normalized RMSE for MORFEO CP, considering the FRFs along the normal direction.

σ_E (%)	r_{MP} %	r_{FP} %	r_{FEP} %
2	2.05	3.03	6.00
3	2.62	3.72	7.40
5	5.60	6.19	10.79
7	8.72	8.92	13.14

Table 7 Normalized RMSE for the LISA optical assembly, considering the FRFs along the input direction.

σ_E (%)	r_{MP} %	r_{FP} %	r_{FEP} %
2	2.07	2.35	6.53
3	3.21	4.19	8.74
5	3.54	4.24	11.03
7	6.25	6.99	13.79

Table 8 Normalized RMSE for the LISA optical assembly, considering the FRFs along the normal direction.

σ_E (%)	r_{MP} %	r_{FP} %	r_{FEP} %
2	1.97	5.52	11.41
3	3.21	8.07	15.21
5	5.62	12.37	20.28
7	10.26	17.19	24.38

The tables suggest that the MP method provides the best overall accuracy, as expected. The FEP method, despite being a strong simplification, provides satisfactory results, not significantly worse than the other methods. These considerations hold true at any uncertainty level and for all case studies analyzed. The FEP results also meet the purpose of this work, which is to provide a tool capable of incorporating material uncertainties in the preliminary stages of a system design while being computationally light and robust. The use of margin factors can translate into RMS errors that go well beyond a few percent.

4.2 Pearson Correlation Coefficient

The Pearson correlation coefficient[10,32,34] measures the linear correlation between two curves, providing a value of their congruence and capturing the trends of the curves (without accounting for their closeness). Given two series a and b that are being compared, the Pearson correlation coefficient ϱ is defined as

$$\varrho = \frac{L\sum_{n=1}^{L} a_n b_n - \sum_{n=1}^{L} a_n \sum_{n=1}^{L} b_n}{\sqrt{L\sum_{n=1}^{L} a_n^2 - \left(\sum_{n=1}^{L} a_n\right)^2}\sqrt{L\sum_{n=1}^{L} b_n^2 - \left(\sum_{n=1}^{L} b_n\right)^2}}, \tag{20}$$

where a_n and b_n are the series values at the nth samples and L represents the total number of samples. In general, the Pearson coefficient may range in value between one and minus one, with

1 being the ideal value.[33] Similarly to what we did for the RMSE, we estimate and compare ϱ for the 1σ standard deviation level of the DFEM (benchmark), MP, FP, and FEP methods.

The Pearson coefficients are computed at all uncertainty levels considered and are shown in Tables 9 and 10 for MORFEO CUFM, Tables 11 and 12 for MORFEO CP, and Tables 13 and 14 for the LISA optical assembly.

Similar to the RMSE conclusions, the tables suggest that the MP method provides the best approximation of the random FRFs due to uncertainty. Despite significant simplifications, the FEP method provides good results.

Table 9 Pearson coefficient for MORFEO CUFM for input-output along parallel directions.

σ_E (%)	ϱ_{MP} %	ϱ_{FP} %	ϱ_{FEP} %
2	99.97	99.96	99.91
3	99.96	99.94	99.82
5	99.83	99.80	99.56
7	99.50	99.51	99.14

Table 10 Pearson coefficient for MORFEO CUFM for input-output along orthogonal directions.

σ_E (%)	ϱ_{MP} %	ϱ_{FP} %	ϱ_{FEP} %
2	99.97	99.94	99.85
3	99.91	99.88	99.74
5	99.76	99.68	99.39
7	99.50	99.41	99.01

Table 11 Pearson coefficient for MORFEO CP for input-output along parallel directions.

σ_E (%)	ϱ_{MP} %	ϱ_{FP} %	ϱ_{FEP} %
2	99.96	99.92	99.89
3	99.97	99.93	99.89
5	99.83	99.74	99.61
7	99.53	99.47	99.27

Table 12 Pearson coefficient for MORFEO CP for input-output along orthogonal directions.

σ_E (%)	ϱ_{MP} %	ϱ_{FP} %	ϱ_{FEP} %
2	99.98	99.94	99.80
3	99.96	99.92	99.69
5	99.80	99.76	99.29
7	99.50	99.48	98.88

Table 13 Pearson coefficient for the LISA optical assembly for input-output along parallel directions.

σ_E (%)	ϱ_{MP} %	ϱ_{FP} %	ϱ_{FEP} %
2	99.98	99.97	99.78
3	99.94	99.88	99.58
5	99.93	99.89	99.31
7	99.76	99.71	98.89

Table 14 Pearson coefficient for the LISA optical assembly for input-output along orthogonal directions.

σ_E (%)	ϱ_{MP} %	ϱ_{FP} %	ϱ_{FEP} %
2	99.98	99.80	99.29
3	99.93	99.58	98.63
5	99.79	98.98	97.34
7	99.27	97.96	95.85

Given the statistical nature of the metric formulation, the Pearson correlation coefficient is checked with a test of hypothesis, assessing also for its significance.[33–36] We associate the null hypothesis H_0 with the case in which there is no correlation between the curves being compared. The two-sided test statistic t_m of the mth Pearson coefficient is

$$t_m = \varrho_m \sqrt{\frac{L-2}{1-\varrho_m^2}}, \tag{21}$$

where ϱ_m is the Pearson coefficient being tested for its significance.

With a significance level α, if the absolute value of the statistic t_m is greater than the corresponding two-sided t-student's distribution value $t_{1-\frac{\alpha}{2},\nu}$ (where ν is the number of DoF and is equal to $L-2$), there is evidence to support that there is a statistically significant correlation between the FRFs being compared. Considering α equal to 1%, the H_0 hypothesis is never accepted, at any uncertainty level and for all case studies, supporting the claim that there is a statistically significant linear correlation between the FRFs being compared.

4.3 Discussion of the FEP Method Performance

Despite the simplifying hypothesis, the FEP method gives results that are valuable and statistically significant. The reasons for these performances can be traced to the modes with higher effective masses.

The effective mass measures the amount of mass moving along each direction for each mode; this is important for realistic models in which the DoF could be many, and not every mode participates at the same level to the deformation of the structure.

The first and second columns of Table 15 show the maximum effective mass along any direction of the first ten modes of MORFEO CP (where θ, η, and ϕ identify the rotations around x, y, and z, respectively), as an example. The third column of Table 15 represents the standard deviation of the frequency of each mode normalized on the frequency itself as a function of the imposed uncertainties on Young's modulus.

The table shows that factor 1/2 applies well to all modes with a high effective mass. The same consideration also holds true for the other systems analyzed. The table suggests that using the FEP method to predict the system response is valuable in the early design of an opto-mechanical system, particularly in providing a straightforward link between Young's modulus and changes in eigenfrequencies.

Table 15 Standard deviations of the frequency of each mode normalized on the frequency itself as a function of the imposed uncertainty on Young's modulus for MORFEO CP. The standard deviations come from the Monte Carlo simulations.

	Effective mass (kg)						σ_f (%)			
Mode	x	y	z	θ	η	ϕ	$\sigma_E = 2\%$	$\sigma_E = 3\%$	$\sigma_E = 5\%$	$\sigma_E = 7\%$
1	0.1	1.9	1.1	94.9	0.6	2.3	1.0	1.5	2.5	3.5
2	0.0	93.6	3.5	1.7	1.7	102.9	1.0	1.5	2.4	3.4
3	70.1	1.4	127.9	0.9	44.5	1.4	1.0	1.4	2.4	3.4
4	118.0	1.1	27.1	0.3	25.9	0.8	0.9	1.4	2.4	3.3
5	14.0	1.0	44.0	0.0	0.0	0.0	0.8	1.2	2.0	2.9
6	0.5	72.2	1.3	0.0	0.0	0.2	0.8	1.2	2.0	2.8
7	0.1	46.8	0.0	0.0	0.0	0.3	0.8	1.2	1.9	2.7
8	11.8	0.3	0.2	0.0	0.1	0.0	0.8	1.2	2.0	2.9
9	4.6	0.0	9.6	0.0	0.1	0.0	0.7	1.1	1.8	2.5
10	0.2	0.9	0.1	0.0	0.0	0.0	0.8	1.2	2.0	2.9

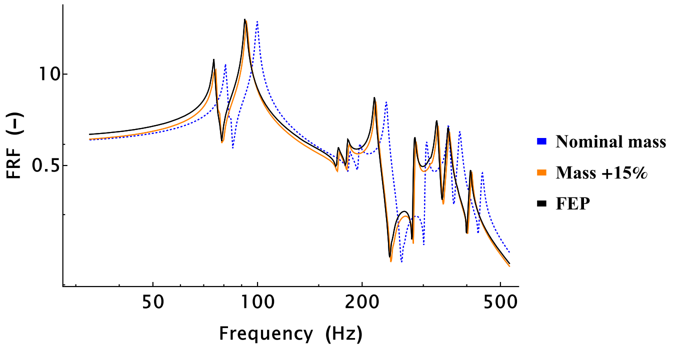

Fig. 9 FRFs along the x direction for MORFEO CUFM. Three curves are included: the blue, black, and orange lines refer to the FRFs computed in the nominal condition, with a 15% mass increment and with the FEP method, respectively.

Finally, we test the FEP method with a different uncertain parameter. Typically, the mass of a system is underestimated by 10% to 20% in the first phases of development. The FEP method can also account for this. In Fig. 9, we show the nominal FRF of MORFEO CUFM (dashed blue curve) and the same FRF when the mass is increased uniformly by 15% (orange curve). The curve generated by the FEP with a −7.5% frequency (black curve) is a good approximation of the modified FRF. Also in this case, the designer can generate a family of curves and use an ensemble FRF for robustness of performance assessments.

5 Conclusions

The dynamics of opto-mechanical systems play a crucial role in ensuring their performance, especially in noisy environments. The natural uncertainty of the physical parameters can be a high risk in the early design phase. Typically, during the initial stages of an opto-mechanical system design, nominal material properties are considered. This approach, however, leads to a lack of robustness and possibly to extensive redesigns following initial testing. Conversely, integrating potential deviations immediately into the analysis proves to be a cumbersome process, often hampered in large projects by issues related to confidentiality and software compatibility.

With a focus on opto-mechanical systems, we propose the frequency envelope propagation method (FEP) that gives a general link from the uncertainty on a parameter to the change in the important eigenfrequencies. The FEP can also be used with models in the modal space, where the dependency on physical parameters is partially lost.

The FEP is tested and validated on three opto-mechanical designs at different uncertainty levels via a comparison with other methods, such as the finite element Monte Carlo simulation (DFEM) and the linear modal perturbation (MP). We also propose a modification to the MP, the frequency propagation method (FP), in which the effect of a parameter change on the eigenfrequencies is linearized neglecting the change in modal shapes.

We conclude that the FEP and FP methods have performances comparable to more exact methods but with a computationally lighter burden. In addition, the FEP gives successfully a straightforward link between a parameter uncertainty and the resulting uncertainty on the eigenfrequencies. This link facilitates the generation of a robust family of FRFs. The FEP method provides a robust and validated tool useful especially in the preliminary stages of a system design, reducing the risk of lengthy iterations. This is important particularly in devices relying on precise optical path lengths or that have tight constraints for modal decoupling.

The research presented here is also an overview of the basics of techniques that account for material parameter uncertainty in the early design phase of large-scale projects.

The future developments of this work include assessing the methods against real measurements on an array of nominally equal systems and extending the technique to uncertainties involving more parameters.

Code and Data Availability

Data sharing is not applicable to this article as no new data were created or analyzed.

References

1. M. W. McElwain et al., “The James Webb Space Telescope Mission: optical telescope element design, development, and performance,” *Publ. Astron. Soc. Pac.* **135**, 058001 (2023).
2. S. Ramsay et al., “The ESO Extremely Large Telescope instrumentation programme,” *Proc. SPIE* **11203**, 1120303 (2020).
3. K. Danzmann et al., “LISA - Laser Interferometer Space Antenna,” Technical Report (2017).
4. A. G. Straume-Lindner and P. Ingmann, “ADM-Aeolus: the first space-based high spectral resolution Doppler wind Lidar,” in *IEEE Int. Geosci. Remote Sensing Symp.* pp. 4969–4974 (2007).
5. M. S. Kompella and R. J. Bernhard, “Measurement of the statistical variation of structural-acoustic characteristics of automotive vehicles,” in *Noise & Vib. Conf. & Expos.*, SAE International (1993).
6. R. H. Lyon, R. G. DeJong, and R. H. Lyon, *Theory and Application of Statistical Energy Analysis*, 2nd ed., Butterworth-Heinemann, Boston, (1995).
7. J. Lu et al., “Uncertainty propagation of frequency response functions using a multi-output Gaussian process model,” *Comput. Struct.* **217**, 1–17 (2019).
8. R. Holzlöhner et al., “Structural, thermal, and optical performance analysis applied to subsystems of the European Extremely Large Telescope,” *J. Astron. Telesc. Instrum. Syst.* **8**(2), 021504 (2022).
9. R. Gilmozzi and J. Spyromilio, “The European Extremely Large Telescope (E-ELT),” *The Messenger* **127**(11), 3 (2007).
10. V. Yotov et al., “Improved Craig–Bampton stochastic method for spacecraft vibroacoustic analysis,” *Acta Astronaut.* **178**, 556–570 (2021).
11. S. De Lellis et al., “Structural uncertainty estimation through a Craig-Bampton stochastic method optimisation in satellites structures,” *J. Sound Vib.* **469**, 115123 (2020).
12. M. Remedia et al., “Integrated semiempirical methodology for microvibration prediction,” *AIAA J.* **53**, 1236–1250 (2015).
13. M. Remedia, G. Aglietti, and G. Richardson, “A stochastic methodology for predictions of the environment created by multiple microvibration sources,” *J. Sound Vib.* **344**, 138–157 (2015).
14. R. R. Craig, Jr and M. C. Bampton, “Coupling of substructures for dynamic analyses,” *AIAA J.* **6**(7), 1313–1319 (1968).
15. A. Abolfathi et al., “Investigating the sources of variability in the dynamic response of built-up structures through a linear analytical model,” *J. Sound Vib.* **387**, 163–176 (2017).
16. A. Calvi, “Uncertainty-based loads analysis for spacecraft: finite element model validation and dynamic responses,” *Comput. Struct.* **83**, 1103–1112 (2005).
17. E. C. Stewart, P. A. Blelloch, and R. N. Coppolino, “Improving accuracy of structural dynamic modification with augmented residual vectors,” in *AIAA Scitech 2019 Forum*, American Institute of Aeronautics and Astronautics, San Diego, California (2019).

18. S. Laborde and A. Calvi, "Spacecraft base-sine vibration test data uncertainties investigation based on stochastic scatter approach," *Mech. Syst. Sig. Process.* **32**, 69–78 (2012).
19. D. Pederbelli, P. Nali, and A. Calvi, "Euclid spacecraft sine vibration test prediction through the virtual shaker testing technique," *J. Spacecr. Rockets* **60**(5), 1517–1526 (2023).
20. G. Cataldo, E. Qian, and J. Auclair, "Multifidelity uncertainty quantification and model validation of large-scale multidisciplinary systems," *J. Astron. Telesc. Instrum. Syst.* **8**, 038001 (2022).
21. S. Uebelhart, D. Miller, and C. Blaurock, "Uncertainty Characterization in Integrated Modeling," in *46th AIAA/ASME/ASCE/AHS/ASC Structures, Structural Dynamics and Materials Conf.* (2005).
22. K. Zhou et al., "Recent advances in uncertainty quantification in structural response characterization and system identification," *Probab. Eng. Mech.* **74**, 103507 (2023).
23. F. DiazDelaO et al., "Stochastic structural dynamic analysis using Bayesian emulators," *Comput. Struct.* **120**, 24–32 (2013).
24. S. H. Lee and W. Chen, "A comparative study of uncertainty propagation methods for black-box type functions," in *Int. Des. Eng. Tech. Conf. Comput. Inf. Eng. Conf. 6 33rd Design Automation Conference, Parts A and B* (2007).
25. L. W. T. Ng and K. E. Willcox, "Multifidelity approaches for optimization under uncertainty," *Int. J. Numer. Methods Eng.* **100**(10), 746–772 (2014).
26. S. Gupta and D. Ghosh, Chap. 5 in *Uncertainty Quantification in Structural Engineering: Current Status and Computational Challenges*, pp. 119–149, World Scientific (2016).
27. B. Mace and P. Shorter, "A local modal/perturbational method for estimating frequency response statistics of built-up structures with uncertain properties," *J. Sound Vib.* **242**, 793–811 (2001).
28. L. Meirovitch, *Fundamentals of Vibrations*, Waveland Press (2010).
29. S. S. Rao, *Vibration of Continuous Systems*, John Wiley & Sons (2019).
30. E. M. A. Redaelli et al., "MAORY/MORFEO at ELT: optomechanical preliminary design," *Proc. SPIE* **12188**, 121883V (2022).
31. M. Colpi et al., "LISA Definition Study Report," (2024).
32. M. W. Liemohn et al., "RMSE is not enough: guidelines to robust data-model comparisons for magnetospheric physics," *J. Atmos. Sol. Terr. Phys.* **218**, 105624 (2021).
33. J. Ren et al., "A comparison of numerical and Lu modeling of water flow and heat transport with laboratory experiments," *Environ. Earth Sci.* **78**, 267 (2019).
34. E. I. Obilor and E. C. Amadi, "Test for significance of Pearson's correlation coefficient," *Int. J. Innov. Math. Stat. Energy Policies* **6**(1), 11–23 (2018).
35. D. C. Montgomery and G. C. Runger, *Applied Satistics and Probability for Engineers*, John Wiley & Sons (2010).
36. A. Papoulis, *Probability and Statistics*, Prentice-Hall, Inc. (1990).

Edoardo Dalla Ricca is a postdoctoral fellow at the University of Trento, Italy. His main research interests include the development of mechatronic technologies for precise space inertial systems for gravitational sensors and Earth observation and the characterization of adhesion in space mechanisms. He has also served as a visiting researcher at Texas A&M University (USA) and has a PhD in mechatronics and systems engineering.

Carlo Zanoni is a senior engineer at the National Institute for Nuclear Physics (INFN) in Italy, where he is responsible for the Gravitational Reference System of the LISA mission: the first gravitational wave observatory in space and a large-class mission approved for launch in 2035. He has been a mechanical engineer at the European Southern Observatory (Germany), developing hardware for the Extremely Large Telescope and a senior fellow at CERN (Switzerland), where he coordinated novel superconducting systems for the upgrade of the Large Hadron Collider. He has also served as a visiting researcher at Stanford University (USA) and Airbus (Germany) and has a PhD in mechanical systems.

Edoardo Maria Alberto Redaelli is a space engineer at the National Institute for Astrophysics (INAF) in Italy. He is responsible for the mechanical design of ground-based astronomical instrumentation for the Very Large Telescope (VLT) and the Extremely Large Telescope (ELT). His main projects include MORFEO, ANDES, and CUBES. He earned his PhD in mechanical engineering, focusing on the use of mechanical alignment and measurement tools for the ultra-precise integration of large opto-mechanical elements in astronomical instruments. During his PhD, he was also a visiting researcher at the European Southern Observatory.